

Numerical investigation of a bio-inspired underwater robot with skeleton-reinforced undulating fins

GUANGYU SHI and QING XIAO*

Department of Naval Architecture, Ocean and Marine Engineering, University of Strathclyde,
Glasgow, G4 0LZ, Scotland, UK

In this paper, the propulsion performance of a bio-inspired underwater robot with a pair of ray-supported undulating pectoral fins is numerically investigated with a fully coupled fluid-structure interaction model. In this model, the flexible fin rays are represented by nonlinear Euler-Bernoulli beams while the surrounding flow is simulated via solving the Navier-Stokes equations. Kinematically, each pectoral fin is activated independently via individually distributed time-varying forces along each fin ray, which imitate effects of tendons that can actively curve the fin rays. We find that the propulsion performance of the bio-inspired robot is closely associated with the phase difference between the leading edge ray and the trailing edge ray of the pectoral fin. The results show that with a symmetrical kinematics, the highest thrust is created when the phase difference is 90 degree while the point maximizing the propulsion efficiency varies with the motion frequency. It is also found that there is a minimum frequency of generating net thrust for a specific parameter setup, which rises as the increase of phase difference. Compared with the symmetrical kinematics, the non-symmetrical kinematics generates more complicated hydrodynamic forces and moments which may be beneficial for the turning maneuver.

*Email address for correspondence: qing.xiao@strath.ac.uk. Tel: +44 01415484779.

1. Introduction

As the growing need for the performance of underwater missions such as ocean exploration, coastal inspection and environmental monitoring, autonomous underwater vehicles (AUVs) are playing an increasingly critical role in conducting these tasks [1]. Despite the wide use of conventional AUVs in ocean engineering, their performance declines significantly at low-speed maneuvering. Besides, the precise station-keeping is difficult to achieve in the presence of drifting currents [2]. To address these issues associated with conventional AUVs, scientists and engineers are seeking solutions from aquatic animals that have diversified into every corner of the ocean after millions of year's evolution [3]. The propulsive mechanisms possessed by many aquatic animals are of great efficiency and maneuverability, which have become the source of inspirations for the design of a new generation of high-performance underwater vehicles.

The locomotion modes of aquatic animals can be generally classified into two categories, namely, body-caudal fin (BCF) mode and median and/or paired fin (MPF) mode [4]. Although most aquatic species adopt the BCF mode to generate thrust, there are still approximately 15% of the fish species exclusively employ the MPF mode for locomotion [2]. Among the MPF locomotion modes, the propulsive mechanisms based on the undulatory fins (e.g., *gymnotiform* and *rajiform*) are attracting increasing attentions from researchers due to the capabilities of vectoring forces and retaining rigid bodies. Figure 1 demonstrates two examples of aquatic swimmers adopting undulating fins for locomotion and the corresponding bio-inspired underwater robots.

Due to the high performance and maneuverability of undulating fin-based locomotion, the kinematics, hydrodynamics as well as the force generation have been studied by previous research. Three different approaches are commonly used in the study of undulating fins, including live animal experiment [5–9], robotic prototype [2,10–14] and computational model [15–17]. With a mechanical prototype, Curet et al. [11] investigated how hydrodynamic forces and swimming speed of the robot change as some critical kinematic variables (e.g., frequency, amplitude and wavelength) vary. Liu et al. [14] examined the effects of fin ray stiffness as well as aspect ratio on the propulsion

performance of an undulating-fin-based robot. They concluded that an increase of ray flexibility leads to a decrease in both thrust and power consumption. But the propulsion efficiency can be improved by flexible rays. Additionally, they also suggested that there could be an optimal aspect ratio for a given fin kinematics. Computationally, Shirgaonkar et al. [15] examined the hydrodynamics of a stationary ribbon fin in still water and found the primary mechanism for thrust production of undulating fin is associated with the generation of a streamwise central jet and other attached vortex rings. Curet et al. [16] investigated the effect of counter-propagating waves with both a computational model and a biomimetic robot. They found that a mushroom-cloud-like flow pattern with an inverted jet was generated by inward counter-propagating waves, which created a high vertical force needed for hovering.

The ability of actively and passively controlling the surface deformation and activation has the potential to improve the propulsion efficiency and maneuverability [18]. Ray-finned fish have multi-degree-of-freedom control over their fins due to the capability of actuating the rays individually. They can modulate their fin deformations to create desired forces [19]. Morphologically, a fin ray consists of a central cartilage pad surrounded by paired, segmented bony elements called hemitrichs, which are connected with tendons at the ends. By pulling the tendons, a hemitrich can slide past the other one, creating a distributed bending moment along the length of a ray. This unique bi-laminar design of the fin rays [20,21] enables the ray-finned fish to have the ability of actively controlling the ray's curvature, which may further enhance their propulsion performance. Youngerman et al. [9] experimentally measured and analyzed the kinematics of a ghost knifefish (*Apteronotus albifrons*) during four locomotor behaviors. They found that ghost knifefish were actively curving their rays in each considered behavior. Apart from the ray-finned fish (*Actinopterygii*), some swimmers belonging to *Elasmobranchii* (e.g., rays and skates) also have active curvature control over their fins. Di Santo et al. [7] studied the effect of swimming speed on the deformation of pectoral fin in the little skate (*Leucoraja erinacea*). They found that at higher speed, the little skate can cup the pectoral fin into the flow, implying the active curvature control and fin stiffening.

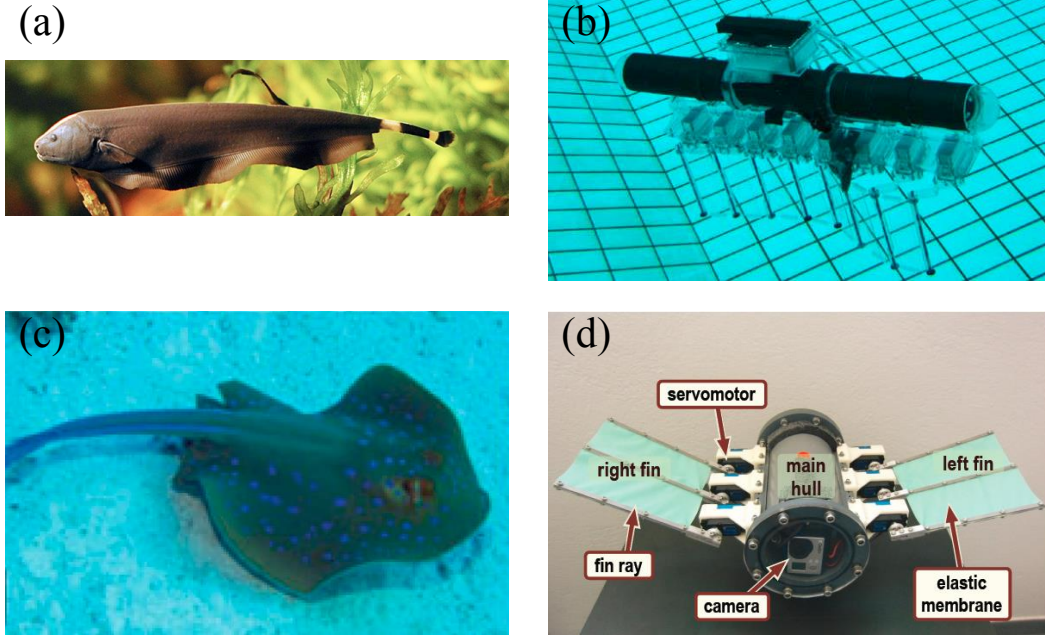


Figure 1 (a) Black ghost knifefish (*Apteronotus albifrons*, gymnotiform). Photograph courtesy of Per Erik Sviland. (b) Nanyang knifefish robot (NYF-I) [22]. (c) Bluespotted ribbontail ray (*Taeniura lymma*, rajiform). Photograph courtesy of Derek Keats. (d) Bio-inspired underwater robot with two undulatory fins [23].

Although the active control over the fin surface widely exists in aquatic animals, it has attracted very limited attention from the scientists and engineers [21,24,25]. Tangorra et al. [26] experimentally tested a mechanical pectoral fin, which was supported by seven flexible, bi-laminar rays. The rays were actuated individually by controlling the nylon tendons attached to the base of each ray. Such a novel design allowed active control over the fin's deformation and motion. Numerically, Alben et al. [20] developed a two-dimensional linear elasticity model of a bi-laminar fin ray. The two hemitriches of the ray were represented by two identical, inextensible beams and the space between them was filled with incompressible linearly elastic material. They found that the ray with tapered tip can produce larger curvature near the tip while the curvature of the uniform ray is localized near the base. However, the interaction with an external fluidic environment was not investigated in their study.

Bearing this in mind, we numerically investigate the propulsion performance of a bio-inspired, skate-like underwater robot with a pair of ray-strengthened pectoral fins in the

present paper. The fluid dynamics around the robot is simulated by solving the Navier-Stokes equations using a finite volume method. The flexible supporting rays are modeled as nonlinear Euler-Bernoulli beams while the constraint from the soft membrane is represented by distributed linear springs connecting neighboring rays. The rays are actuated by distributed external forces, mimicking the pulling effect from the tendons. The external load can modify/adjust the bending curvature of the fin rays individually and lead them to bend into the flow whereas the rays with purely passive deformation can only conform according to the surrounding fluid. This distinctive feature of the fin rays is rarely considered in previous papers. The objective of the present work is to investigate the propulsion performance of a bio-inspired underwater robot which has the ability of actively controlling the curvature of its fin rays. The novelty of the present study lies in the consideration of both the fluid-structure interaction and the active curvature control of ray-supported undulatory pectoral fins, which is rarely considered in previous numerical studies. The present work may provide some useful inspirations for the design of bio-inspired underwater robots.

The rest of this paper is organized as follows: in section 2, the geometry, material property, kinematics and actuation of the simplified underwater robot are described and the parameters which characterize the performance are defined. In section 3, the governing equations and numerical methods used in the present fluid-structure interaction solver are briefly introduced. In section 4, the numerical results, including fin deformation, force generation and near-body flow field are presented. The conclusions are drawn in the final section.

2. Problem Description

In the present study, a simplified bio-inspired underwater robot which is composed of a body and a pair of ray-strengthened pectoral fins (as shown in Figure 2 (a)) is numerically studied. The body is idealized as a rigid plate. The length, width and thickness of the body are denoted as L_{body} , W_{body} and h respectively, where $W_{body} = L_{body}/3$ and $h = 0.004L_{body}$. Each pectoral fin is modeled as a rectangular-shaped membrane supported by N evenly distributed flexible rays. The two fins are identical and have the

same dimensions as the body, i.e., $L_{fin} = L_{body}$, $W_{fin} = W_{body}$ and $H_{fin} = h$. Each ray is structurally represented by a nonlinear Euler-Bernoulli beam with uniform flexibility. The non-dimensional bending stiffness is defined as $K_i \equiv E_i I / \rho U_\infty^2 L_{ray}^3$, ($i = 1, \dots, N$), where $N = 11$, E_i is the Young's modulus of the i^{th} ray, I is the second moment of inertia, ρ is the fluid density, U_∞ is the freestream velocity and $L_{ray} = W_{fin}$ is the length of the ray. The mass ratio is defined as $m_i^* \equiv \rho_{s,i} h / \rho L_{ray}$, where $\rho_{s,i}$ is the density of the i^{th} ray. In the present work, the bending stiffness of all rays is selected to be $K_i = 1.0$ unless specified and the mass ratio of the ray are chosen as $m_i^* = 0.2$.

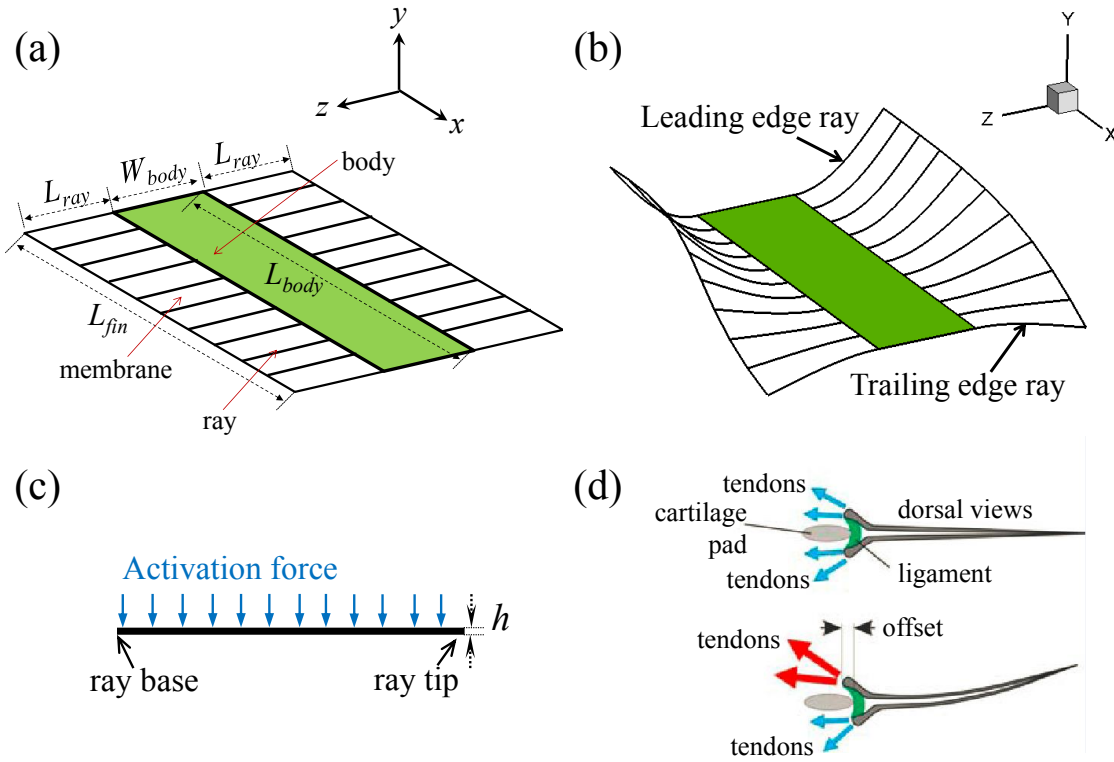


Figure 2 (a) Simplified underwater robot model in the present study. (b) Illustration of the deformation of the pectoral fin. (c) Schematic view of the actuation of a ray, where the distributed external force models the pulling effect of the tendons. (d) Dorsal view of a fin ray with two hemitrichs [20].

In reality, the membrane connecting neighboring rays imposes complicated constraints on the dynamics of fin rays. However, in the present study, the bending stiffness of the membrane is assumed to be negligible, i.e., it cannot sustain any bending but only

stretching and compression. Therefore, the constraints provided by the membrane are simplified as distributed linear springs between the neighboring rays. As we are not aiming at entirely duplicating the biological details, the spring constant is selected to be $0.02 \rho U_\infty^2 L_{fin}$ based on the numerical tests, i.e., the springs are sufficiently rigid to prevent excessive expansion yet still flexible enough to allow large deformation.

Kinematically, the body is fixed in space and all the basal ends of the ray are clamped to the body. With a uniform incoming flow, this is equivalent to the situation that the body is swimming at a constant speed. This approach is also widely used in similar biomimetic studies [19,27]. Each ray is actuated by independent external loads, mimicking the pulling effect of the tendons at the basal end of the ray (see Figure 2 (c) and (d)). The external force acting on the i^{th} ray can be expressed as

$$F_i(t) = F_0 \sin(2\pi f t - \varphi_i) \quad (1)$$

where F_0 is the magnitude of the external force, f is the frequency, φ_i is the phase and t is the time. In this paper, we choose $\varphi_1 = 0$ and $\varphi_i = \varphi_d(i - 1)/(N - 1)$, where φ_d is the phase lag between the leading edge ray and trailing edge ray. F_0 is assumed to be uniform along the ray and its value is chosen based on numerical tests, i.e., the desired deformations can be accomplished while maintaining the numerical stability. Here, F_0 is selected to be $2 \rho U_\infty^2 L_{fin}^2$. The reduced frequency based on the fin length L_{fin} , frequency f and incoming flow velocity U_∞ is defined as $f_r \equiv f L_{fin} / U_\infty$. It should be noted that the present study is not aimed at duplicating the exact activation mechanism of real fish fins as shown in Figure 2 (d). Instead, we are inspired by the ability of actively changing the curvature of the ray. The external force is only used to achieve the desired undulating deformation.

The propulsion performance of the fin is characterized by the mean thrust coefficient $\overline{C_T}$, the mean amplitude of the vertical force coefficient $\overline{C_Y}$, the mean lateral force coefficient $\overline{C_Z}$, the mean x-moment coefficient $\overline{C_{MX}}$, the mean y-moment coefficient $\overline{C_{MY}}$, the mean z-moment coefficient $\overline{C_{MZ}}$, the mean power expenditure coefficient $\overline{C_P}$, and the propulsion efficiency η . These mean values are evaluated by averaging the instantaneous

coefficients over one motion period T . \widetilde{C}_Y is defined as the average of the absolute values of the maxima and minima of the vertical force coefficient within one motion period. The instantaneous thrust coefficient is defined as

$$C_T(t) = \frac{-F_X(t)}{0.5\rho U_\infty^2 L_{fin}^2}, \quad (2)$$

where $F_X(t)$ is the x -component of the instantaneous hydrodynamic force $\mathbf{F}(t)$. The thrust direction is along the negative x -axis, thus a minus sign is included in Eq. (2).

Similarly, we have

$$\begin{aligned} C_Y(t) &= \frac{F_Y(t)}{0.5\rho U_\infty^2 L_{fin}^2}, \\ C_Z(t) &= \frac{F_Z(t)}{0.5\rho U_\infty^2 L_{fin}^2}, \\ C_{MX}(t) &= \frac{M_X(t)}{0.5\rho U_\infty^2 L_{fin}^3}, \\ C_{MY}(t) &= \frac{M_Y(t)}{0.5\rho U_\infty^2 L_{fin}^3}, \\ C_{MZ}(t) &= \frac{M_Z(t)}{0.5\rho U_\infty^2 L_{fin}^3}, \\ C_P(t) &= \frac{P(t)}{0.5\rho U_\infty^3 L_{fin}^2}, \end{aligned} \quad (3)$$

where $F_Y(t)$ and $F_Z(t)$ are the components of the instantaneous hydrodynamic force $\mathbf{F}(t)$ in y and z directions respectively. $M_X(t)$, $M_Y(t)$ and $M_Z(t)$ are the moments about the axis parallel to the x -, y -, and z -axis and through the center of the body respectively. $P(t)$ is the instantaneous hydrodynamic power, which is evaluated as

$$P(t) = \iint_S \mathbf{F}(\mathbf{x}, t) \cdot \mathbf{V}_g(\mathbf{x}, t) d\mathbf{x}, \quad (4)$$

where $\mathbf{V}_g(\mathbf{x}, t)$ is the moving velocity of the fin. In reality, the input power from the actuation should be higher than the hydrodynamic power. However, here we assume that the power loss in the fin system is negligible, i.e., the input power from the muscle is very close to the hydrodynamic power calculated using Equation (4). Therefore, the propulsion efficiency η can be approximated as

$$\eta = \frac{\overline{C_T}}{\overline{C_P}} \quad (5)$$

3. Mathematical Formulation and Numerical Methods

The current proposed problem involves the interaction between the flexible ray-supported fins and the surrounding flow, which needs to be addressed using a fluid-structure interaction solver tailored for this specific problem. The present fluid-structure interaction solver includes three key modules: a fluid dynamics solver, a structural dynamics solver and a fluid-structure coupling procedure.

The fluid dynamics solver numerically solves the unsteady compressible Navier-Stokes equations, which is written in its integral form

$$\frac{\partial}{\partial t} \iiint_{\Omega} \mathbf{U} dV + \iint_{\partial\Omega} \mathbf{G} d\mathbf{S} - \iint_{\partial\Omega} \mathbf{H} d\mathbf{S} = 0, \quad (6)$$

where $\mathbf{U} = (\rho, \rho\mathbf{v}, \rho E)^T$ is the conservative variable vector, Ω is the control volume, $\partial\Omega$ is the boundary surface enclosing the volume, and \mathbf{S} is the surface vector in outward direction. ρ is the fluid density, \mathbf{v} is the velocity vector and E is the total energy. \mathbf{G} and \mathbf{H} are the convective and diffusive flux vectors, respectively.

The fluid equation Eq. (6) is discretized by a cell-centred finite volume method based on an overset, multi-block structured grid system [28,29]. With a structured grid method, the fluid domain is divided into an array of hexahedral cells. Each grid cell is uniquely denoted by three computational coordinates i, j, k . For each hexahedral cell (i, j, k) , the conservation laws are applied and the following semi-discrete form can be derived

$$\frac{\partial}{\partial t} (\mathbf{U}_{i,j,k} \Delta\Omega_{i,j,k}) - \mathbf{R}_{i,j,k} = \mathbf{D}_{i,j,k}, \quad (7)$$

where $\mathbf{R}_{i,j,k}$ measures the convective and diffusive fluxes entering the hexahedral cell through its surface. $\mathbf{D}_{i,j,k}$ denotes the artificial viscosity that is used to stabilize the scheme and eliminate the spurious numerical oscillations [30].

For time-dependent simulations, the dual-time stepping algorithm [31] is employed for

the temporal integration, where equation (7) is reformulated as a steady-state problem with a pseudo-time \tilde{t} :

$$\frac{\partial}{\partial \tilde{t}} \mathbf{U}^{n+1} = \frac{1}{\Delta \Omega^{n+1}} \tilde{\mathbf{R}}(\mathbf{U}^{n+1}), \quad (8)$$

where

$$\begin{aligned} \tilde{\mathbf{R}}(\mathbf{U}^{n+1}) &= \mathbf{R}(\mathbf{U}^{n+1}) + \mathbf{D}(\mathbf{U}^{n+1}) \\ &- \frac{3(\mathbf{U}\Delta\Omega)^{n+1} - 4(\mathbf{U}\Delta\Omega)^n + (\mathbf{U}\Delta\Omega)^{n-1}}{2\Delta t}. \end{aligned} \quad (9)$$

Equation (8) is then integrated by a hybrid multistage Runge-Kutta scheme. At each time step, the domain connectivity is accomplished by an overset grid assembler based on an implicit hole cutting technique [29].

In the structural part, the dynamics of the nonlinear Euler-Bernoulli beam is governed by [32]

$$\begin{aligned} m_s \frac{\partial^2 \mathbf{x}}{\partial t^2} + K_b \frac{\partial^4 \mathbf{x}}{\partial s^4} - K_s \frac{\partial}{\partial s} \left\{ \left[1 - \left(\frac{\partial \mathbf{x}}{\partial s} \cdot \frac{\partial \mathbf{x}}{\partial s} \right)^{-0.5} \right] \frac{\partial \mathbf{x}}{\partial s} \right\} \\ = \mathbf{F}_f + \mathbf{F}_{sp} + \mathbf{F}_{ac}, \end{aligned} \quad (10)$$

where \mathbf{x} is the instantaneous position of the ray, and s ($0 < s < L_{ray}$) is the Lagrangian coordinate. $m_s = \rho_s h$ is the mass per unit length, where ρ_s is the density of the fin rays. $K_b \equiv Eh^3/12$ and $K_s \equiv Eh$ represent the bending and stretching stiffness respectively. On the right hand side, \mathbf{F}_f denotes the fluid load and \mathbf{F}_{sp} represents the force exerted by the connecting linear springs which model the constraints from the collagenous membrane. \mathbf{F}_{ac} is the distributed force along the beam, which models the pulling effect by the tendons at the basal end of the ray (see Figure 2 (c)). The material damping effect is considered by replacing the Young's modulus E in K_b and K_s with $E(1 + \sigma \partial/\partial t)$, where σ denotes the structural damping coefficient. In all present simulations, we select $\sigma = 2L_{fin}/U_\infty$. Here, the material damping factor is considered as a very small value, which is only used to stabilize the beam model. Therefore, its effect on the power consumption is assumed to be negligible.

At the basal end ($s = 0$) of each ray, a fixed boundary condition is imposed,

$$\begin{aligned} \mathbf{x}(0, t) &= \mathbf{x}(0, 0) \\ \frac{\partial \mathbf{x}(0, t)}{\partial s} &= [1, 0]^T. \end{aligned} \quad (11)$$

At the ray tip, the free boundary condition is employed,

$$\begin{aligned} K_b \frac{\partial^3 \mathbf{x}}{\partial s^3} - K_s \left[1 - \left(\frac{\partial \mathbf{x}}{\partial s} \cdot \frac{\partial \mathbf{x}}{\partial s} \right)^{-0.5} \right] \frac{\partial \mathbf{x}}{\partial s} &= 0 \\ \frac{\partial^2 \mathbf{x}}{\partial s^2} &= 0 \end{aligned} \quad (12)$$

It is noted that the external forces have no influence on the boundary conditions of the nonlinear beam model. Equation (10), together with boundary conditions (11) and (12), are discretized using a second-order finite difference method and the resulting linear system is solved with an iterative Gauss-Seidel method [32,33].

In the present algorithm, the Navier-Stokes solver is coupled with the nonlinear beam model via a partitioned framework. Compared with a strongly coupled algorithm, which requires iterations within each time step, a loosely coupled method needs only a single data exchange between the fluid solver and structural solver in each time step so that it significantly reduces the computational expense. Despite the numerical stability issue associated with loosely coupled methods [34], this approach is still favoured due to its simplicity and efficiency. Since the caudal fin model is completely three-dimensional and requires plenty of computational time, a loosely coupled approach known as conventional serial staggered procedure [35] is used in the present work. A suitable value of mass ratio should be used in order to maintain the stability of this coupling scheme [34]. Due to the non-conformity between the fluid grid and structural grid, interpolations of fluid forces and structural displacements must be performed at the fluid-structure interface. For the force interpolation, both the fluid grid nodes on the wet boundary of the body and the structural grid nodes are firstly projected to a common planar plane, on which a bilinear interpolation is then performed [28]. Despite the simplicity of this interpolation method, the force conservativeness is not retained at the interface. The structural displacements are transferred to the fluid mesh by a conservative method known as constant volume tetrahedron [36,37].

It is worth noting that no turbulence model is used in the present study, i.e., the flow is assumed to be laminar. In relatively low Reynolds number regimes (below or in the order of 10^3), the turbulence effect may play an insignificant role in the flow field. For these scenarios, laminar flow models are usually used for biomimetic problems (see examples in [27,38–40]). Additionally, the flow model is formulated with the compressible Navier-Stokes equations. To ensure that the compressibility is negligibly small, the freestream Mach number (defined as $M_\infty = U_\infty/a_\infty$, where U_∞ and a_∞ are flow velocity and speed of sound of the freestream respectively) is chosen to be 0.06, which is far below the critical value for pronounced compressibility effect ($M = 0.3$) but still sufficiently large for numerical stability. Besides, the local Mach numbers in the complete computational domain are monitored to guarantee that they are below the critical value. Therefore, for the present flow solver, Mach number is just a parameter and a change of its value within a reasonable range will not change the simulation results. The present compressible flow solver has been successfully applied to study different incompressible flow problems in our previous work [28,41–45].

4. Results

The problem depicted in Figure 2 (a) is solved using the fluid-structure interaction solver described in Section 3. The computational domain used in the present paper are the same as that in our previous publication [28]. The Reynolds number based on the length of the fin is $Re = 6000$ unless specified. The height of the first grid layer off the wall (Δy) is choosing to be $\Delta y = 0.001L_{fin}$.

The present fluid-structure interaction solver has been validated via several canonical cases in our previous paper [28]. Specifically, the flow solver was examined by simulating the flow past a three-dimensional circular cylinder while the structural solver was validated by reproducing the 1st-order and 2nd-order bending modes of a cantilever beam. The coupled solver was then examined by predicting the dynamic response of an elastic cantilever immersed in the wakes of a square cylinder. All these cases showed good agreements with the results from literature.

A sensitivity study to the mesh density is carried out to demonstrate the suitability of the grid resolution. Three grids with different densities are generated, which are termed as Fine Mesh (5 million cells), Medium Mesh (3.7 million cells) and Coarse Mesh (2.8 million cells). Particularly, the numbers of grid point along the fin are 101, 81 and 61 for the Fine, Medium and Coarse meshes respectively. Figure 3 illustrates the instantaneous thrust and vertical force coefficients obtained from three different meshes at $\varphi_d=180$ degree. It is seen that the result from Medium Mesh is almost the same to that from Fine Mesh, indicating the convergence of the flow field. The pressure coefficient ($C_{pre} \equiv \frac{p-p_\infty}{0.5\rho U_\infty^2}$) contours from different mesh resolutions are demonstrated in Figure 4, from which we can see that little difference between the pressure contours can be observed. Based on this sensitivity study, the Medium Mesh is used for the rest simulations of the present paper.

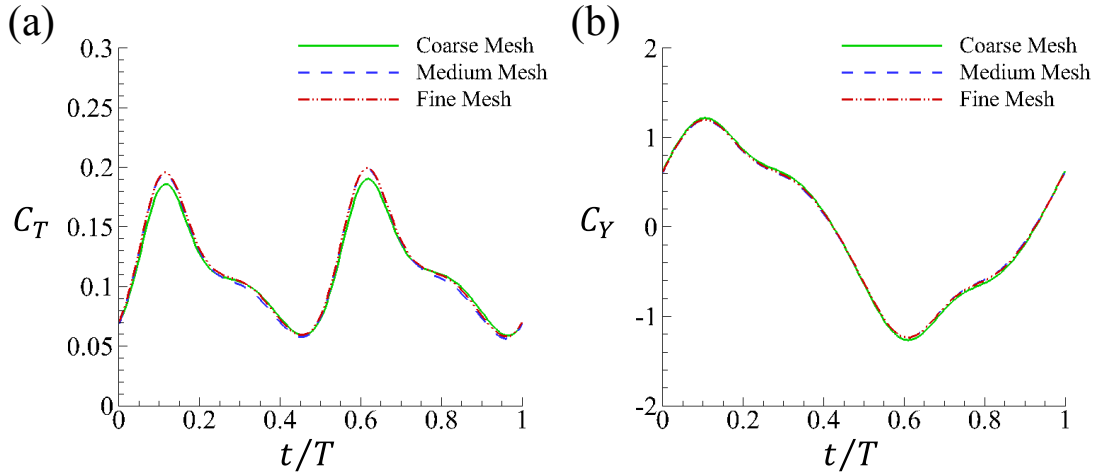


Figure 3 Sensitivity study of the present flow solver to the CFD mesh density. $\varphi_d=180$ and $f_r=1.2$.

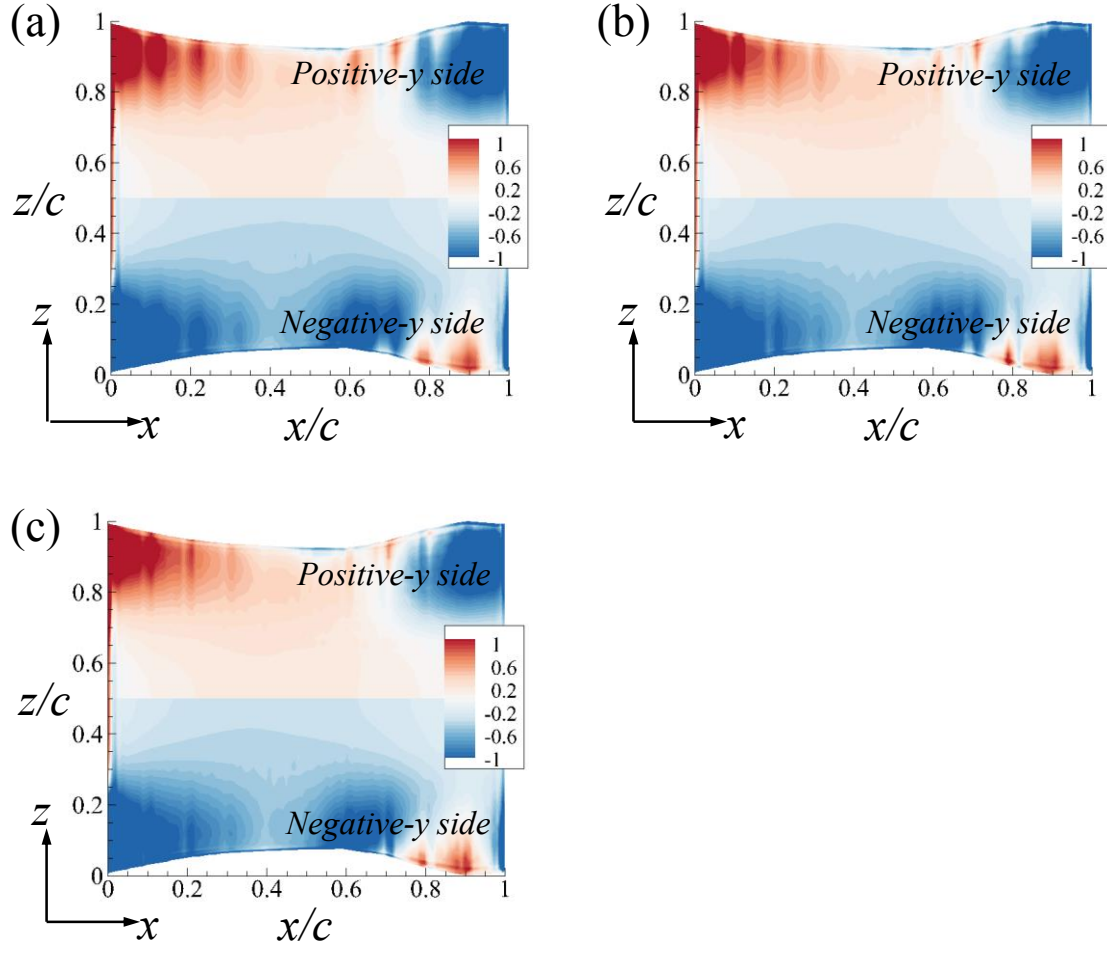


Figure 4 Pressure coefficients (C_{pre}) distributions at both sides of the robot at $t = 0$ for three different meshes, (a) Coarse Mesh, (b) Medium Mesh, and (c) Fine Mesh. $\varphi_d=180$ degree, $f_r=1.2$.

4.1 Fin deformation and near-body flow field of symmetric fin kinematics

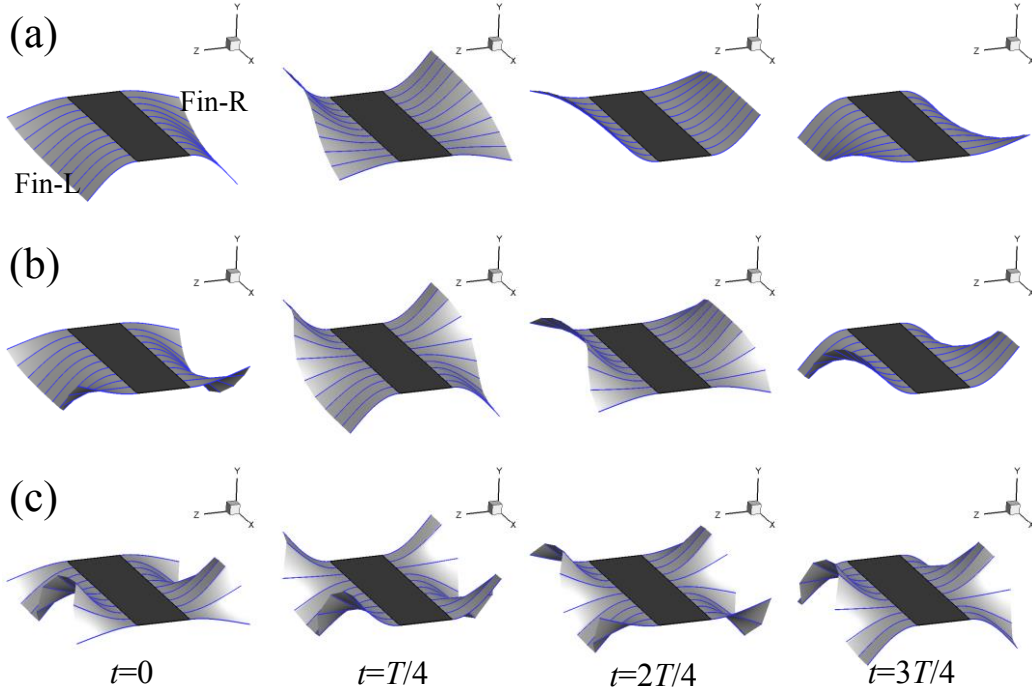


Figure 5 Typical 3D fin deformations within one motion period, (a) $\varphi_d=90$, (b) $\varphi_d=180$, (c) $\varphi_d=360$. $f_r=1.2$.

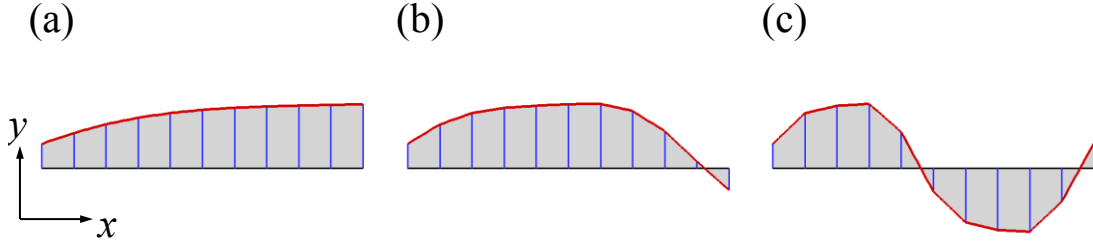


Figure 6 Lateral view of the undulating fin's deformation pattern at $t = T/2$, (a) $\varphi_d=90$, (b) $\varphi_d=180$, (c) $\varphi_d=360$. $f_r=1.2$.

Typical deformations of the undulating pectoral fins within one motion period are demonstrated in Figure 5. The two fins are labeled as Fin-L (left fin) and Fin-R (right fin) respectively. It is seen that with symmetric fin kinematics, the fin deformation patterns are also symmetrical against the middle line of the body. For small phase difference value ($\varphi_d=90$ degree), the pectoral fins actually undergo flapping motions rather than

undulating motions. As the increase of the phase difference, the undulating motions of the fins are more pronounced, particularly when $\varphi_d=360$ degree. The undulating patterns of the fins can be better seen from the lateral views of the robot, which are demonstrated in Figure 6. As seen from this figure, there exists a clear traveling wave along the pectoral fin at $\varphi_d=360$ degree.

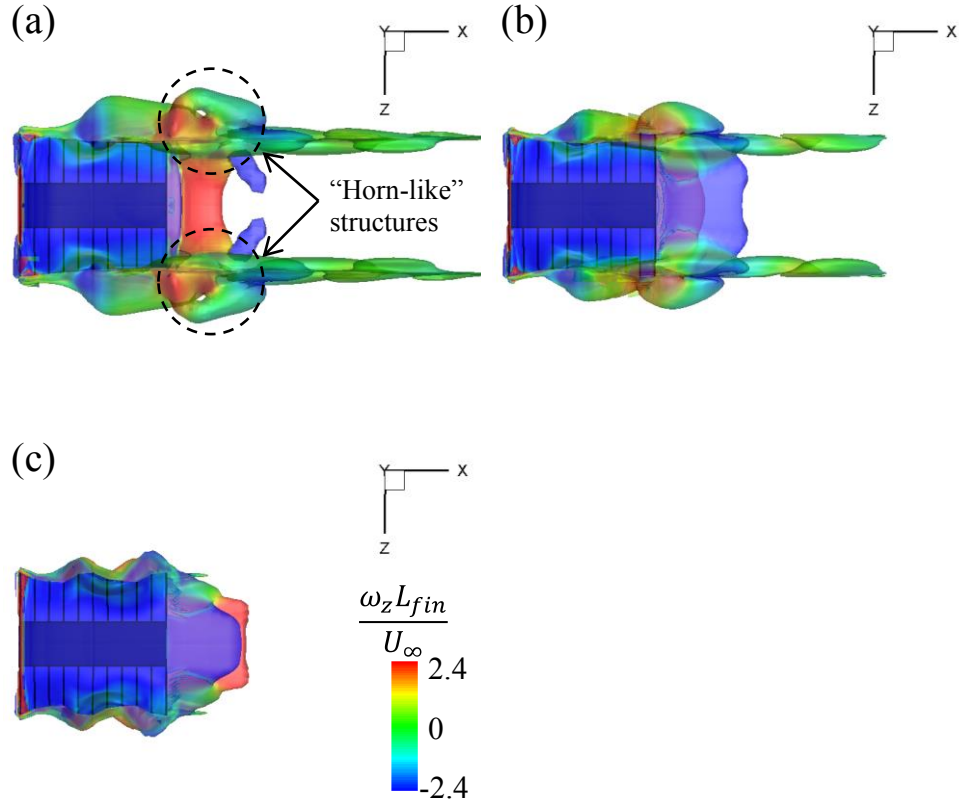


Figure 7 Top views of the iso-surfaces of the normalized vorticity magnitude
 $(\|\omega\| = L_{fin}\sqrt{\omega_x^2 + \omega_y^2 + \omega_z^2}/U_\infty=3)$ behind the robot at $t=0$. The iso-surfaces are coloured using
normalized z-vorticity. (a) $\varphi_d=90$; (b) $\varphi_d=180$; (c) $\varphi_d=360$. $f_r=1.2$.

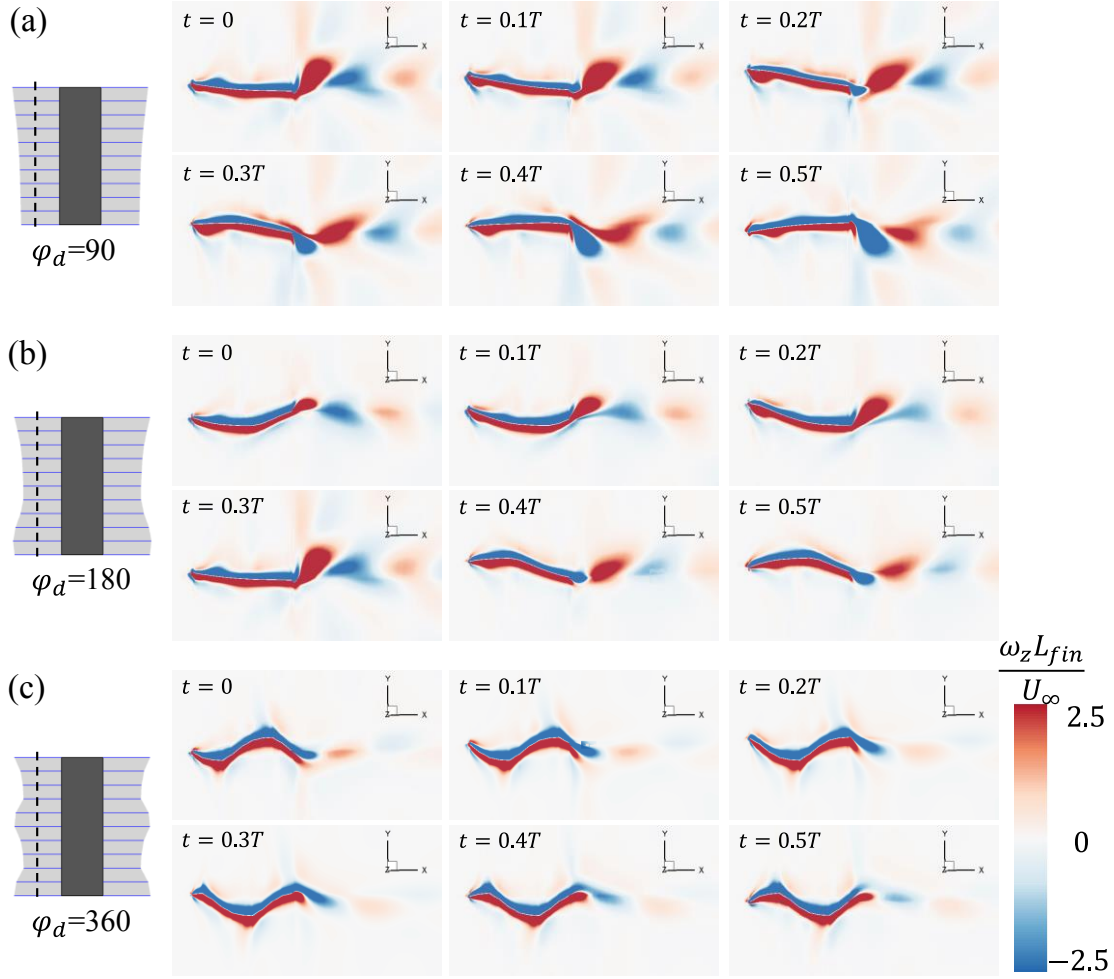


Figure 8 Flow vorticity of slice $z = 0.6L_{ray}$ of Fin-L within half motion period, (a) $\varphi_d=90$, (b) $\varphi_d=180$, and (c) $\varphi_d=360$. $f_r=1.2$.

The iso-surfaces of the normalized vorticity magnitude ($\|\omega\| = 3$) behind the bio-inspired robot are demonstrated in Figure 7. It is seen that the flapping motion at $\varphi_d=90$ degree creates extended wake structures at both side and behind the pectoral fins when they are compared with those produced by the undulating motion at $\varphi_d=360$ degree. Besides, the flapping motion generates “horn-like” wake structures that are not observed at higher phase difference values as demonstrated in Figure 7. The vortex shedding behind the pectoral fin can be more clearly observed in Figure 8. At $\varphi_d=90$ degree, stronger counter-clockwise and clockwise trailing edge vortices (TEVs) are generated and shed into the wake alternatively, whilst the trailing edge vortices become weaker at $\varphi_d=180$ degree. When the phase difference value reaches 360 degree, where the pectoral fin forms a

complete trailing wave (the wave length equals one fin length), no clear trailing edge vortex is observed, which also implies less thrust force will be created in this case, which will be discussed in later section. It is also observed that the flow separates at the fin's surface for all three φ_d values shown here. The flow separation will lead to pressure difference between the two sides of the pectoral fin. Figure 9 shows the pressure coefficient distributions at both sides of the robot at $\varphi_d=90$ and 360 degrees. It is clearly seen that the flapping motion ($\varphi_d=90$) creates significantly larger pressure difference, which may contribute to the thrust generation if appropriately reoriented (see Figure 11 (a)). On the other hand, the larger pressure difference also creates larger vertical force (see Figure 11 (b)), implying more power expenditure. In contrast, the pressure difference generated by the undulating motion ($\varphi_d=360$) is significantly smaller, as demonstrated in Figure 9 (b), which may attribute to relatively slow flow traveling speed along the fin's surface.

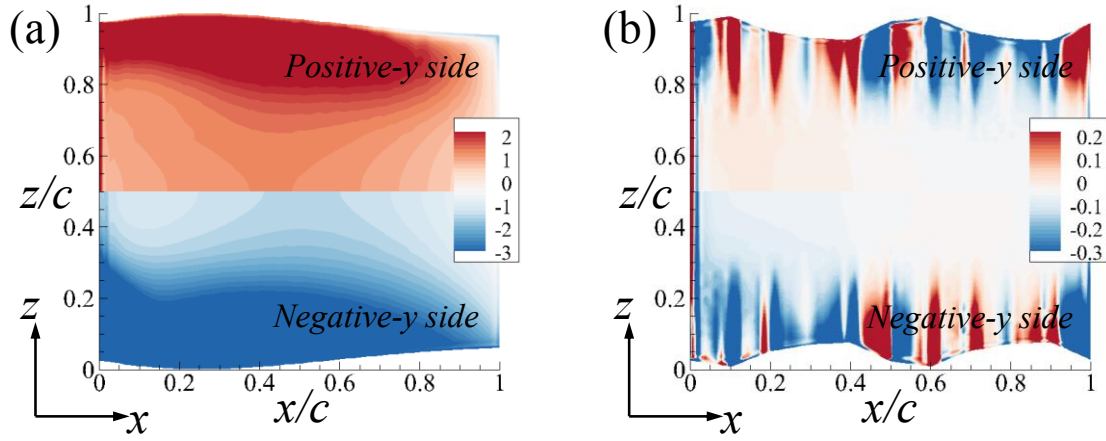


Figure 9 Pressure coefficients (C_{pre}) distributions at both sides of the robot for $\varphi_d=90$ (a) and 360 degrees (b) at $t=0.2T$, $f_r=1.2$. Note that the legend scales of plot (a) and (b) are different.

4.2 Force generation and propulsion efficiency of symmetric fin kinematics

Time averaged thrust coefficient C_T , mean amplitude of vertical force coefficient $\widetilde{C_Y}$ and propulsion efficiency η as functions of φ_d at different reduced frequencies are summarized in Figure 10. The three reduced frequencies are selected to be large enough to generate positive net thrust force, yet not too high to cause numerical instabilities. For all three motion frequencies considered here, the thrust force rises first and then decreases with the increase of the phase difference between the leading and trailing edge rays and the peak value is achieved at $\varphi_d=90$ degree, which corresponds to a wavelength of $4L_{fin}$. The mean amplitude of vertical force coefficient descends monotonously as φ_d increases from 0 to 360 degree, indicating the possible decrease of power expenditure. The propulsion efficiency undergoes a similar trend as the thrust, however, with the peak values accomplished at different φ_d for different reduced frequencies. Specifically, the highest propulsion efficiencies are reached at $\varphi_d=90, 135$ and 180 degrees for $f_r = 0.8, 1.0$ and 1.2 respectively. Previous experimental study of an undulating fin [11] found that the largest thrust force is produced when the wave length is half of the fin's length, which is different from the present study. This difference may be attributed to different aspects. The fin in the present study has an aspect ratio of 0.33 while the aspect ratio of the fin used in the experiment of Curet et al. [11] is around 0.1. Besides, Curet et al. [11] carried out a self-propelled study which is also distinct from the present work. Despite of the lowest thrust force produced by the undulating motion at $\varphi_d=360$ degree, it requires the least power input as well, which may be advantageous under certain circumstances.

The time histories of C_T and C_Y for $\varphi_d=90$ and 180 degrees at $f_r = 1.2$ are demonstrated in Figure 11. One obvious effect of increasing φ_d from 90 degree to 180 degree is the reduction in the generation of thrust peaks. It is seen that two much higher thrust peaks are produced within one motion period at $\varphi_d=90$ degree compared with the case of $\varphi_d=180$ degree. Another effect is the significant reduction in the vertical force generation (force in y -direction), as shown in Figure 11 (b). This leads to a substantial decrease in power expenditure coefficient. The decreasing rate of the power expenditure is higher than that of the thrust force, leading to an increase in propulsion efficiency, as observed in Figure 10 (c).

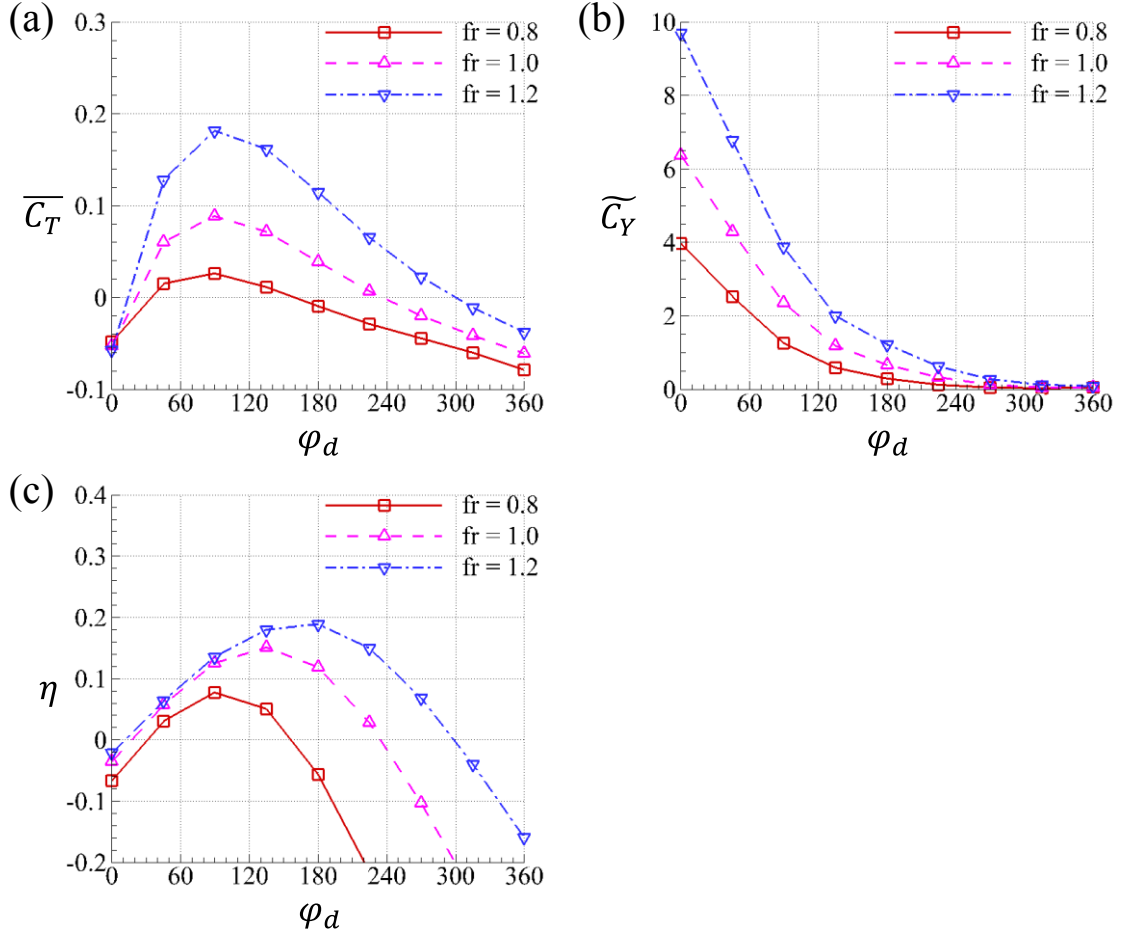


Figure 10 Time averaged thrust coefficients, time-mean amplitudes of vertical force coefficient and propulsion efficiency as functions of the phase difference φ_d at different reduced frequencies.

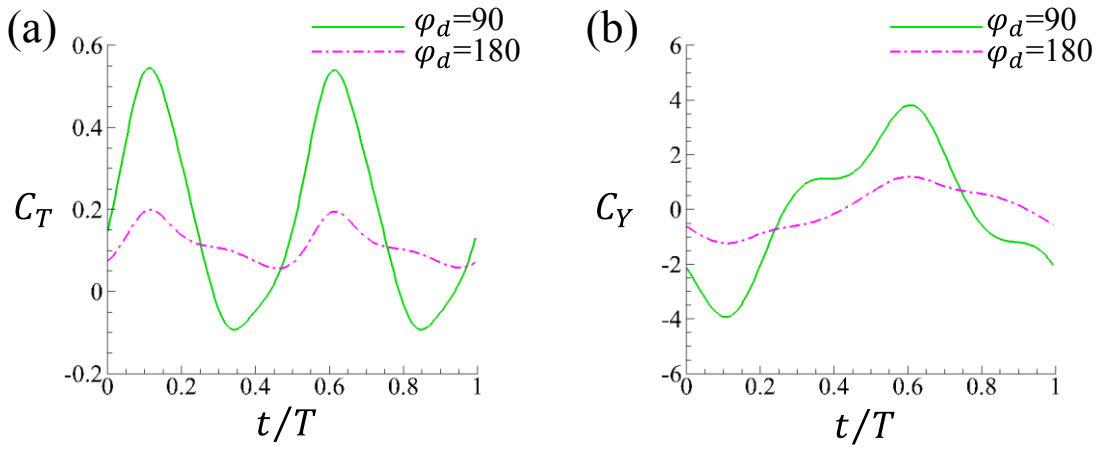


Figure 11 Instantaneous C_T and C_Y within one motion period at two various phase difference values.
 $f_r = 1.2$.

4.3 Effect of structural flexibility

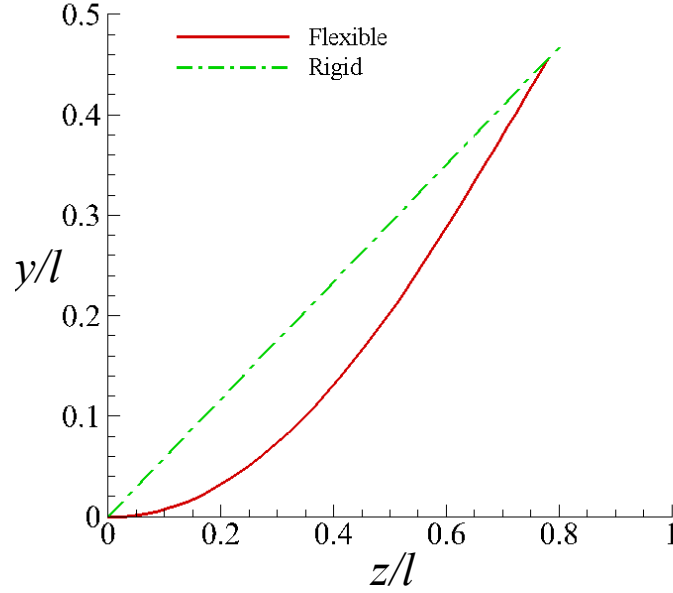


Figure 12 Schematic view of the deformations of the present flexible ray with actively controlled curvature and a rotational rigid ray.

Figure 12 illustrates the difference between the flexible ray in the present work and a rotational rigid ray. The present flexible ray is actuated by a distributed external force which imitates the pulling effects of the muscles. This kind of activation leads to an actively-controlled curvature along the ray, i.e., the slope of the ray varies significantly from the ray base to the ray tip. However, for a rigid ray with the same effective rotational angle, the slope along the ray remains unchanged. In addition, the actively-controlled ray is curved into the direction of motion, thus is also different from the case of purely passive bending in response to the surrounding fluid. This type of curvature changing is also observed in previous study of a live knifefish [9].

Figure 13 demonstrates the time histories of C_T and C_Y for rigid and flexible rays at three various φ_d values. The rotational angle of the rigid case is chosen to be the same as the effective rotational angle of the flexible case in order to have a reasonable comparison. As shown in Figure 13, the fins of flexible rays with active curvature control generate

considerable higher thrust force with a slightly increase in vertical force, especially for cases when $\varphi_d=90$ and 180 degree.

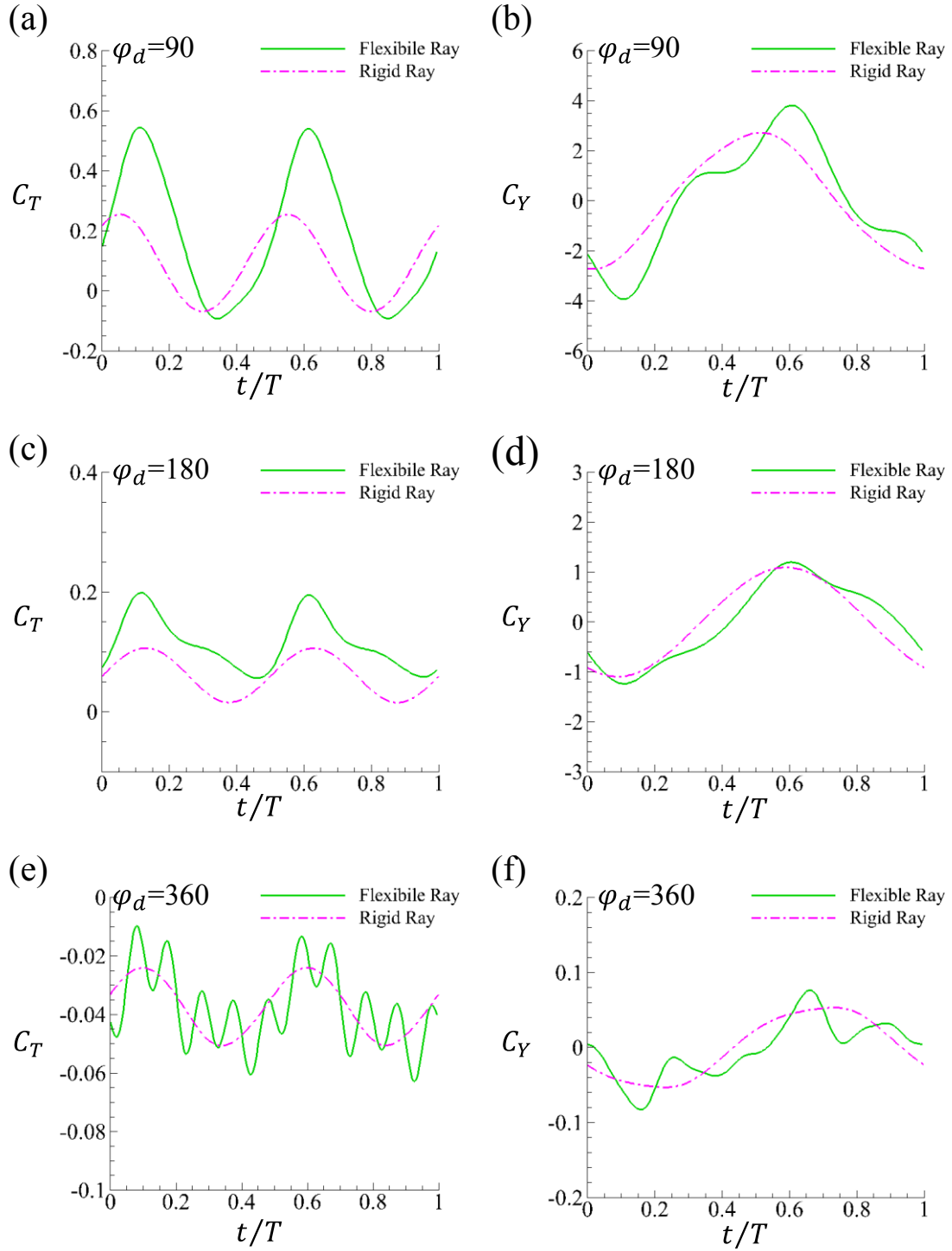


Figure 13 Instantaneous C_T and C_Y within one motion period for rigid and flexible rays at various phase difference values. $f_r=1.2$.

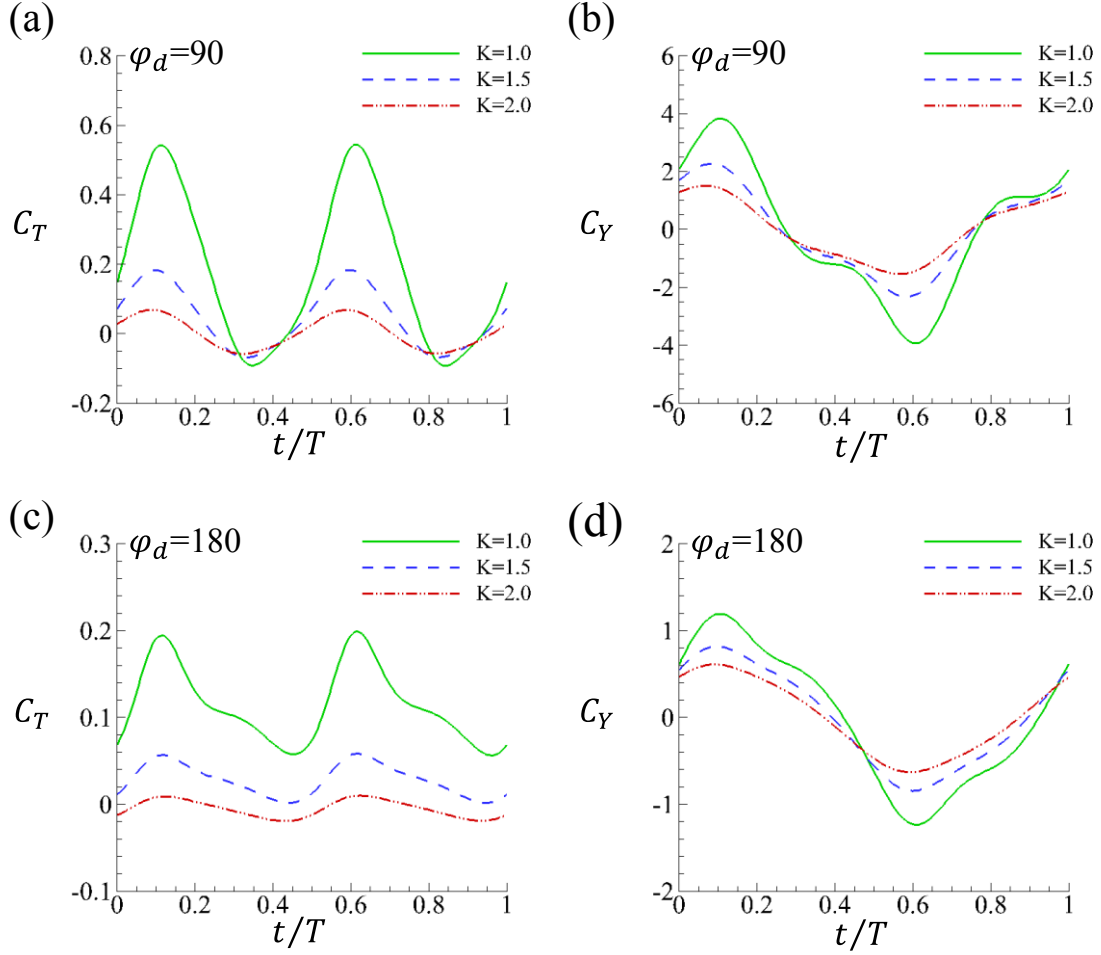


Figure 14 Instantaneous C_T and C_Y within one motion period at three different flexibilities. $K=1.0$ is the default bending stiffness in the present study. $f_r=1.2$.

Figure 14 shows the instantaneous C_T and C_Y at three different bending stiffness values. Both the thrust and vertical forces decline as the decrease of flexibility for both $\varphi_d=90$ and 180 degree. As observed from Figure 15, the decrease of the flexibility while keeping the magnitude of external force is equivalent to reducing the effective rotational angle of the rays, which results in a reduction of thrust generation [11].

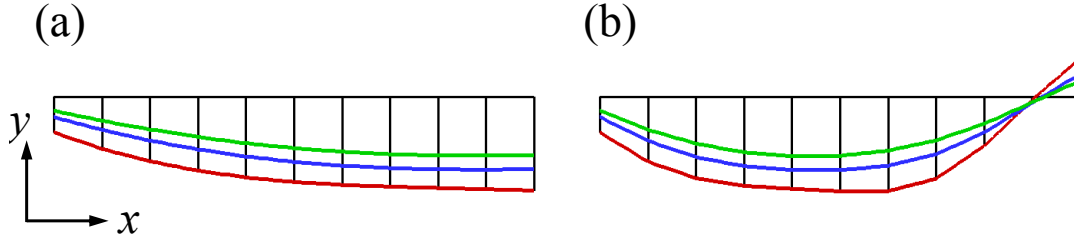


Figure 15 Lateral view of the undulating fin's deformation pattern at $t = 0$, (a) $\varphi_d=90$, (b) $\varphi_d=180$. $f_r=1.2$. Red line: $K=1.0$, blue line: $K=1.5$, and green line: $K=2.0$.

4.4 Effect of non-symmetric kinematics

To examine the effects of non-symmetrical kinematics on the performance of this bio-inspired robot, two additional simulation cases are performed. In the first case (Case I), the phase difference value of Fin-R is 90 degree ($\varphi_d=90$) while for Fin-L, the phase difference is 180 degree ($\varphi_d=180$). In the second case (Case II), the phase differences of both Fin-R and Fin-L are 90 degree, but the phase distribution of Fin-L is reversed while the phase distribution of Fin-R is the same as that of symmetric kinematics case. For both Case I and Case II, the reduced frequency is $f_r = 1.2$ and Reynolds number is $Re = 6000$.

Figure 16 demonstrates the time histories of C_T , C_Y and C_Z of Fin-L, Fin-R and body for Case I and II. It is seen that non-symmetrical kinematics leads to more complicated force generations on the pectoral fins. The forces generated in three directions by Fin-L and Fin-R are no longer symmetrical, which will create moments in x-, y- and z-directions. For symmetrical fin kinematics, the total force along z-axis is zero because the two fins generate forces of the same magnitude but in opposite directions. Due to the non-symmetrical kinematics, the forces in z-axis have different magnitudes, which lead to a net force in z-direction. Compared with Case I, Case II not only creates non-equal thrust forces, but also in opposite directions. In particular, Fin-R generates net thrust while Fin-L creates net drag with larger magnitude. This leads to a larger rotational moment along y-direction, as shown in Figure 17 (b), indicating faster turning maneuvering will be achieved compared with Case I.

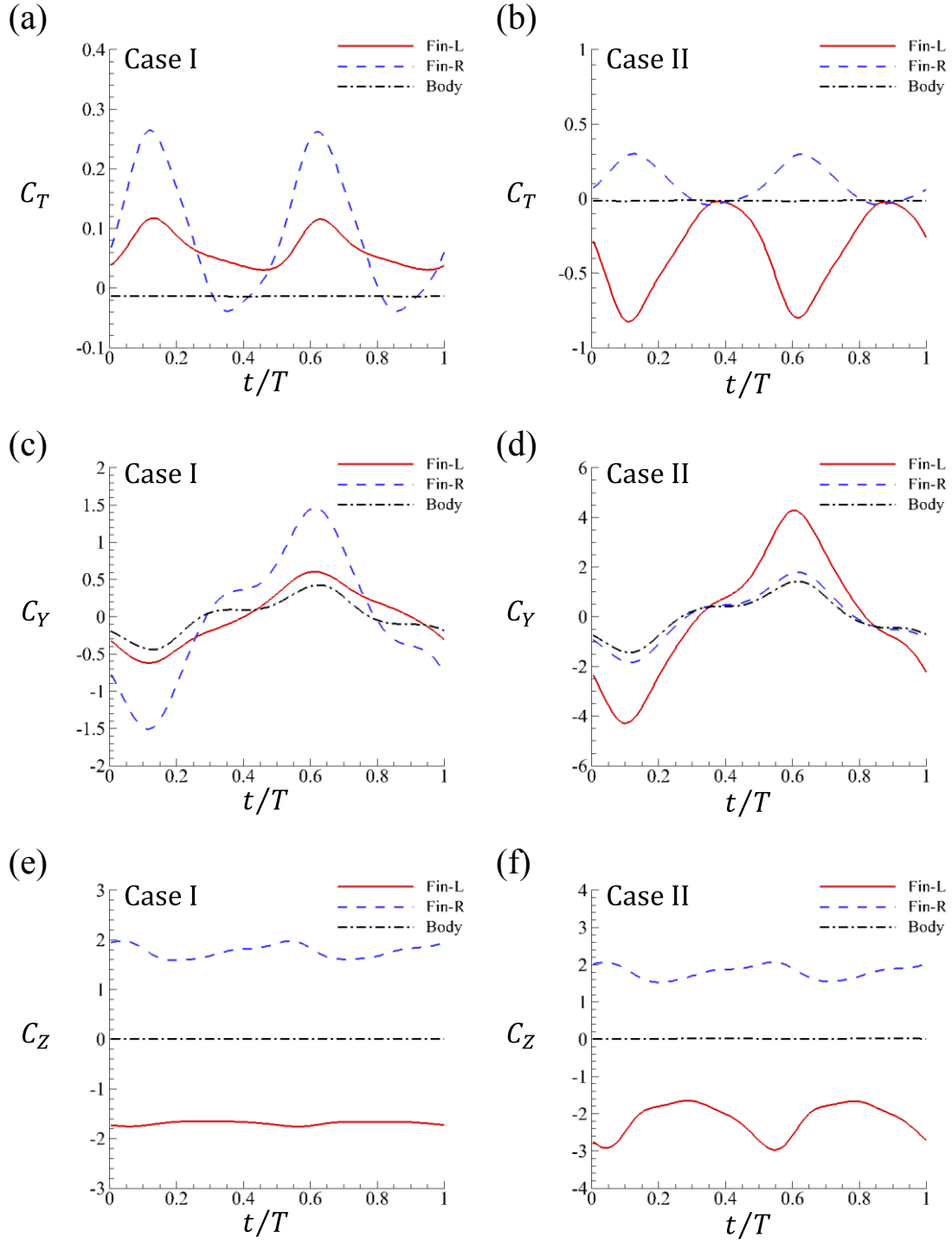


Figure 16 Instantaneous C_T , C_Y and C_Z within one motion period for Case I and Case II.

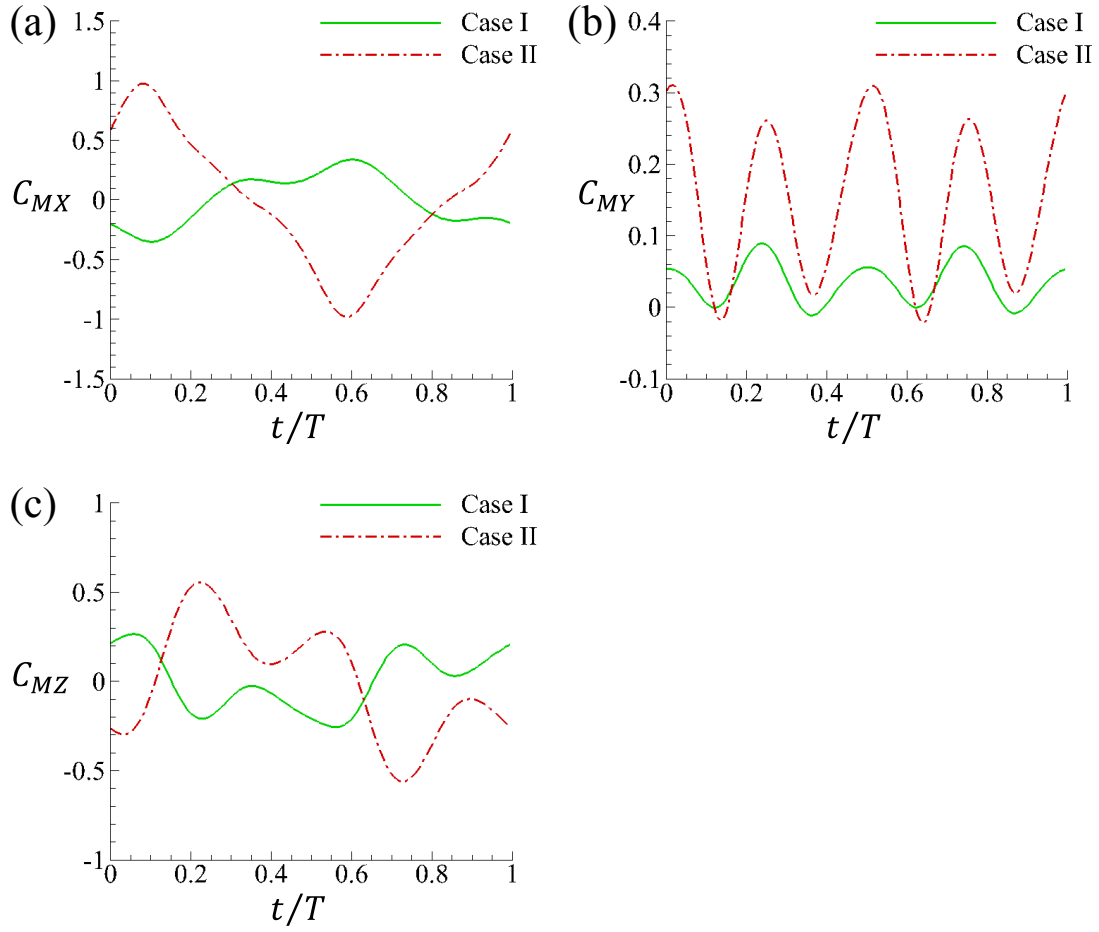


Figure 17 Time histories of x-, y- and z-moment coefficients for Case I and Case II.

Table 1 The time-averaged moment coefficients for Case I and Case II.

	$\overline{C_{MX}}$	$\overline{C_{MY}}$	$\overline{C_{MZ}}$
Case I	-0.0017	0.0343	0.0010
Case II	-0.0003	0.1497	0.0007

Figure 17 demonstrates the instantaneous moment coefficients in three directions for Case I and Case II and the time-averaged values are depicted in Table 1. Both cases produce considerable moments in all three directions and Case II generates relatively higher amplitudes. It is also observed from Table 1 that for both cases, the time-averaged moments in x- and z-directions over one motion cycle are close to zero whereas the time-averaged y-moments have considerable values, which indicates that the x- and z-

moments may cause some periodical rolling and pitching motions of the robot, but the eventual consequence of the non-symmetrical kinematics studied here is the turning maneuver. Figure 18 illustrates the instantaneous C_T and C_Y of Fin-L and Fin-R for Case I at symmetric and non-symmetric actuations. Compared with symmetric kinematics, the force generation is slightly influenced by the interaction of the two fins with different kinematics.

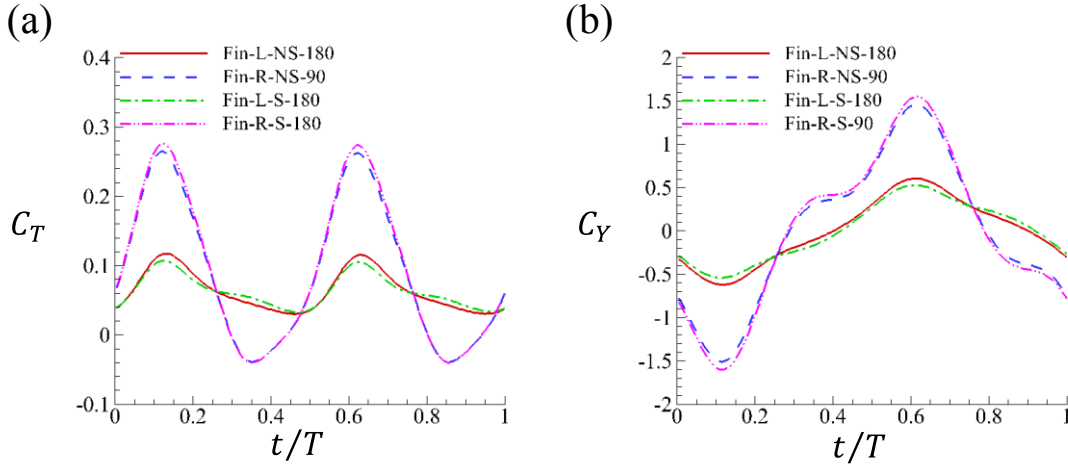


Figure 18 Comparison of the instantaneous C_T and C_Y of Fin-L and Fin-R within one motion period at symmetric and non-symmetric kinematics. Case I at $f_r=1.2$.

4.5 Effect of Reynolds number

Up to this point, our simulations are carried out at a fixed Reynolds number ($Re = 6000$). The effect of Reynolds number on the performance of the underwater robot is examined by performing the simulations at two additional Reynolds numbers ($Re = 300, 1000$). The two pectoral fins have symmetrical kinematics and the reduced frequency f_r is fixed at 1.2. The time averaged values of thrust, mean amplitude of vertical force coefficients and propulsion efficiency as functions of φ_d are demonstrated in Figure 19. It is observed that for the Reynolds numbers considered here, both the thrust and propulsion efficiency have been seen significant enhancements as the increase of Reynolds number. It is also seen that the differences of the mean amplitude of vertical force coefficient between various Reynolds numbers are marginal, especially when compared with those of thrust force.

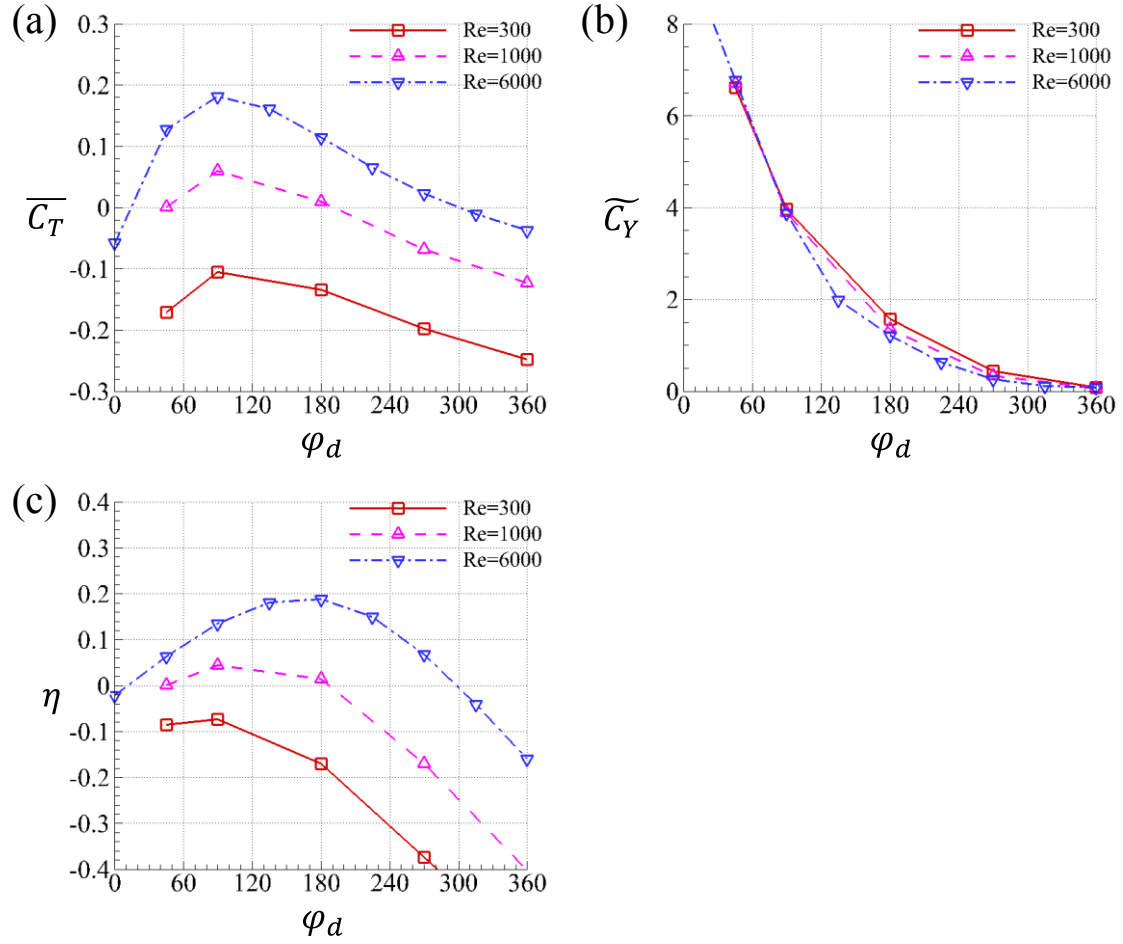


Figure 19 Time averaged thrust coefficients, time-mean amplitudes of vertical force coefficient and propulsion efficiency as functions of the phase difference φ_d at different Reynolds numbers. $f_r=1.2$.

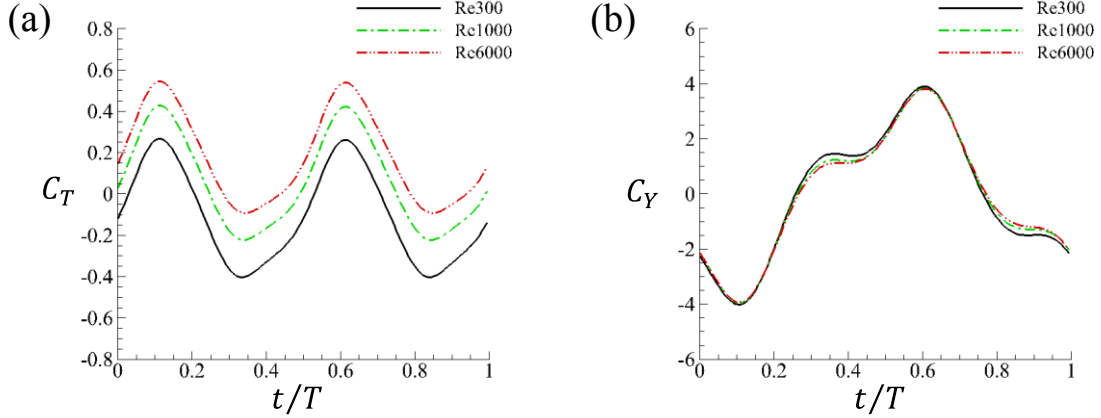


Figure 20 Instantaneous C_T and C_Y within one motion period at different Reynolds numbers. $f_r=1.2$ and $\phi_d=90$ degree.

The time histories of C_T and C_Y within one motion period at different Reynolds numbers are shown in Figure 20. All cases at different Reynolds numbers produce both thrust and drag within one motion period. The drag accounts for higher percentage than the thrust at low Reynolds number ($Re=300$) while larger thrust force is produced at higher Reynolds number ($Re=6000$).

Flow vorticity of slice $z = 0.6L_{ray}$ of Fin-L at $t = 0.5T$ for different Reynolds numbers are shown in Figure 21 (a) and (b). It is observed that stronger trailing edge vortex is generated in the higher Reynolds number case, while the lower Reynolds number case has significantly thicker shear layer, which may be attributed to the more dominated effect of the viscosity. The pressure distributions at both sides of the robot at $t = 0.5T$ are demonstrated in Figure 21 (c) and (d), from which we can see that only subtle differences can be observed, which may explain why the vertical force coefficients for the two cases are very similar to each other (see Figure 20 (b)). This also indicates that the larger shear stress in the lower Reynolds number case may be the primary reason for the increase of the drag force (see Figure 20 (a)).

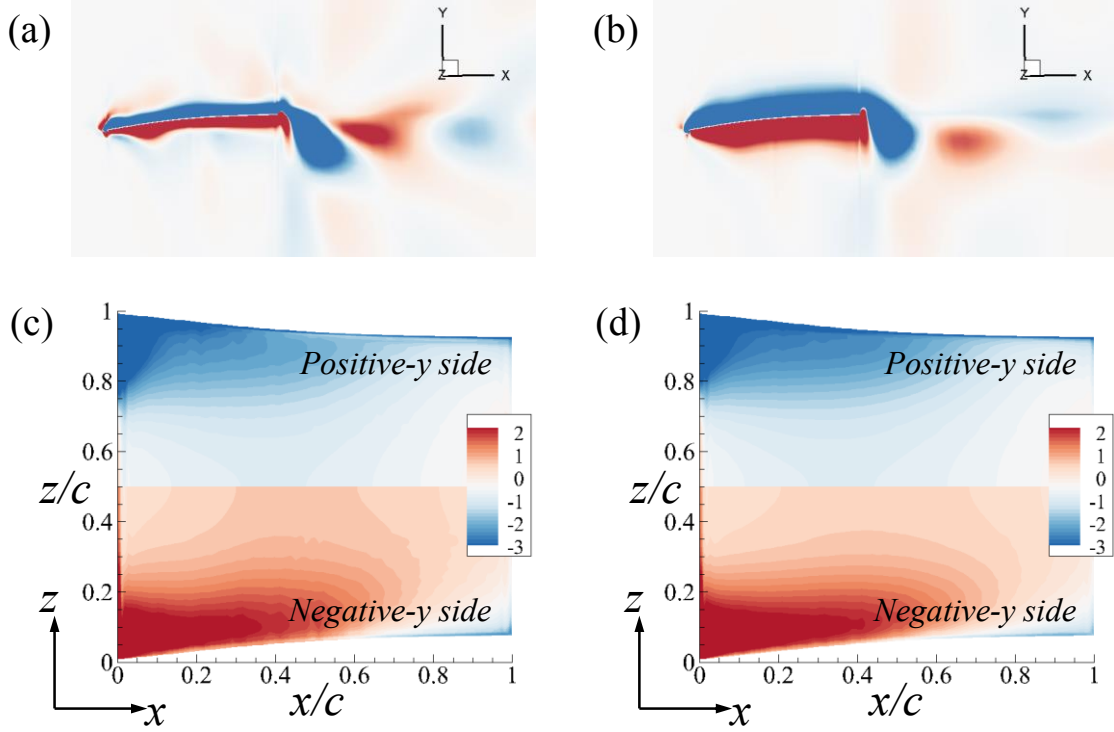


Figure 21 Flow vorticity of slice $z = 0.6L_{ray}$ of Fin-L (a) (b), and pressure coefficient distributions at both sides of the robot at $t=0.5T$ (c) (d). (a) (c) $Re=6000$, and (b) (d) $Re=300$. $f_r=1.2$ and $\varphi_d=90$ degree.

5. Conclusions

Ray-finned fish utilize their flexible fins as control surfaces to accomplish propulsion, station-keeping and maneuvering. The fins are structurally composed of a thin and soft membrane embedded with bony rays, resulting in a skeleton-strengthened bio-membrane system. Such a bio-system enables fish to have multi-degree-of-freedom control over the deformation and force generation of the fin.

In the present paper, we numerically examine the propulsion performance of a biomimetic robot with two sided pectoral fins, which are supported by flexible rays with actively controlled curvatures. The fin rays are activated individually by time-varying distributed forces along each ray, which mimics the pulling effect from the tendons attached at the basal end of each ray. By controlling the phase difference (φ_d) between

the leading edge and trailing edge rays, the pectoral fins can achieve a flapping motion (smaller phase difference) as well as an undulating motion (larger phase difference). The present results demonstrate that for all three motion frequencies considered in this work, the largest thrust is generated when $\varphi_d=90$ degree (corresponding to a wave length of $4L_{fin}$), where the pectoral fins are undergoing flapping motions. The maximum propulsion efficiency, in contrary, is accomplished at different φ_d values for various motion frequencies. Specifically, the peaks of propulsion efficiency are achieved at smaller φ_d values for lower frequencies. Additionally, undulating motion creates significantly smaller pressure differences between the upper and lower sides of the fin, thereby leading to a significant decrease in power expenditure. By employing different φ_d values or reversing the phase distribution, the pectoral fins can generate more complicated hydrodynamic forces and moments. Specifically, non-equal thrust forces are created by the left and right fins, which creates considerable moments in all three directions. However, the x- and z-moments averaged over one motion cycle are close to zero, implying the moments created in these two directions may lead to periodical rolling and pitching motions of the robot. Moreover, the non-symmetrical kinematics also generates to a non-zero lateral force in z-direction, which, together with the considerable net time-averaged y-moment, can be beneficial to the turning maneuver of the robot.

Generally, the motion of the ray-supported fin can be categorized into flapping mode and undulating mode, according to the wave number existing along the fin. The present study suggests that the largest thrust force is produced by flapping mode (corresponding wave number is 0.25). However, this may not be a general conclusion for all different morphologies. An experimental study of Curet et al. [11] using a robotic knifefish found that the highest thrust was achieved at a wave number of two. As discussed in section 4.2, the difference may be caused by the aspect ratio of the fin. In the present work, the aspect ratio of the fin is 0.33 while the aspect ratio of Curet et al. [11] is 0.1. Therefore, we anticipate that for ray-strengthened fins with larger aspect ratios, flapping mode may produce better propulsion performance, but for fins with smaller aspect ratios, better performance may be achieved by undulating mode. Besides, undulating mode may require more rays for actuation, e.g., the anal fin of the weakly electric ghost knifefish

(*Apteronotus albifrons*) is composed of approximately 150 individual rays [9], which enables the existence of multiple traveling waves along its fin. The present study also suggests that undulating mode needs much less power expenditure than flapping motion, which may be a significant advantage of undulating mode.

Another important feature of fish fin is the ability of actively controlling the curvature and bending stiffness of the rays [9,20,21,46]. The actively controlled ray is able to curve into the flow, i.e., the bending direction of the ray is the same as its moving direction. This is significantly different with the rigid and passively deformed rays. The rigid ray does not change its curvature while the passively deformed ray bends in the direction opposite to the moving direction. It has been found in the present study that such a curvature change can augment the thrust production of the pectoral fin, especially at smaller φ_d values. Tangorra et al. [26] designed and tested a biomimetic pectoral fin with a novel actuation mechanism inspired by bluegill sunfish. However, the effects of active control over the curvature as well as the bending stiffness are still not fully studied and understood, which requires more work in the future research.

Acknowledgements

The first author would like to thank China Scholarship Council (CSC) and University of Strathclyde for the financial support during his study in the United Kingdom. Results were partially obtained using the ARCHIE-WeSt High Performance Computer (www.archie-west.ac.uk) based at the University of Strathclyde.

Reference

- [1] R. Salazar, V. Fuentes, A. Abdelkefi, Classification of biological and bioinspired aquatic systems: A review, *Ocean Eng.* 148 (2018) 75–114.
<https://doi.org/10.1016/j.oceaneng.2017.11.012>.

- [2] M. Sfakiotakis, J. Fasoulas, M.M. Kavoussanos, M. Arapis, Experimental investigation and propulsion control for a bio-inspired robotic undulatory fin, *Robotica*. 33 (2015) 1062–1084. <https://doi.org/10.1017/s0263574714002926>.
- [3] G. V. Lauder, E.G. Drucker, Morphology and experimental hydrodynamics of fish fin control surfaces, *IEEE J. Ocean. Eng.* 29 (2004) 556–571. <https://doi.org/10.1109/JOE.2004.833219>.
- [4] M. Sfakiotakis, D.M. Lane, J.B.C. Davies, Review of Fish Swimming Modes for Aquatic Locomotion, *IEEE J. Ocean. Eng.* 24 (1999) 237–252. file:///Z:/Commercial/Current_Projects/14001/Research_Literature/Fish_Swimming_Techniques.pdf.
- [5] E.L. Blevins, G. V. Lauder, Rajiform locomotion: three-dimensional kinematics of the pectoral fin surface during swimming in the freshwater stingray *Potamotrygon orbignyi*, *J. Exp. Biol.* 215 (2012) 3231–3241. <https://doi.org/10.1242/jeb.068981>.
- [6] V. Di Santo, C.P. Kenaley, Skating by: low energetic costs of swimming in a batoid fish, *J. Exp. Biol.* 219 (2016) 1804–1807. <https://doi.org/10.1242/jeb.136358>.
- [7] V. Di Santo, E.L. Blevins, G. V. Lauder, Batoid locomotion: effects of speed on pectoral fin deformation in the little skate, *Leucoraja erinacea*, *J. Exp. Biol.* 220 (2017) 705–712. <https://doi.org/10.1242/jeb.148767>.
- [8] Z.J. Taylor, A. Liberzon, R. Gurka, R. Holzman, T. Reesbeck, F.J. Diez, Experiments on the vortex wake of a swimming knifefish, *Exp. Fluids*. 54 (2013) 54–57. <https://doi.org/10.1007/s00348-013-1588-1>.
- [9] E.D. Youngerman, B.E. Flammang, G. V. Lauder, Locomotion of free-swimming ghost knifefish: Anal fin kinematics during four behaviors, *Zoology*. 117 (2014) 337–348. <https://doi.org/10.1016/j.zool.2014.04.004>.
- [10] T. Hu, L. Shen, L. Lin, H. Xu, Biological inspirations, kinematics modeling, mechanism design and experiments on an undulating robotic fin inspired by *Gymnarchus niloticus*, *Mech. Mach. Theory*. 44 (2009) 633–645. <https://doi.org/10.1016/j.mechmachtheory.2008.08.013>.

- [11] O.M. Curet, N.A. Patankar, G. V. Lauder, M.A. MacIver, Mechanical properties of a bio-inspired robotic knifefish with an undulatory propulsor, *Bioinspiration and Biomimetics*. 6 (2011) 026004. <https://doi.org/10.1088/1748-3182/6/2/026004>.
- [12] I.D. Neveln, R. Bale, A.P.S. Bhalla, O.M. Curet, N.A. Patankar, M.A. MacIver, Undulating fins produce off-axis thrust and flow structures, *J. Exp. Biol.* 217 (2014) 201–213. <https://doi.org/10.1242/jeb.091520>.
- [13] H. Liu, O.M. Curet, Propulsive performance of an under-actuated robotic ribbon fin, *Bioinspir. Biomim.* 12 (2017) 36015. <https://doi.org/10.1088/1748-3190/aa7184>.
- [14] H. Liu, B. Taylor, O.M. Curet, Fin Ray Stiffness and Fin Morphology Control Ribbon-Fin-Based Propulsion, *Soft Robot*. 4 (2017) 103–116. <https://doi.org/10.1089/soro.2016.0040>.
- [15] A.A. Shirgaonkar, O.M. Curet, N.A. Patankar, M.A. MacIver, The hydrodynamics of ribbon-fin propulsion during impulsive motion, *J. Exp. Biol.* 211 (2008) 3490–3503. <https://doi.org/10.1242/jeb.019224>.
- [16] O.M. Curet, N.A. Patankar, G. V. Lauder, M.A. Maciver, Aquatic manoeuvring with counter-propagating waves : a novel locomotive strategy, *J. R. Soc. Interface*. 8 (2011) 1041–1050.
- [17] M.M. Rahman, Y. Toda, H. Miki, Computational Study on a Squid-Like Underwater Robot with Two Undulating Side Fins, *J. Bionic Eng.* 8 (2011) 25–32. [https://doi.org/10.1016/S1672-6529\(11\)60003-6](https://doi.org/10.1016/S1672-6529(11)60003-6).
- [18] G. V. Lauder, Fish locomotion: recent advances and new directions, *Ann. Rev. Mar. Sci.* 7 (2015) 521–545. <https://doi.org/10.1146/annurev-marine-010814-015614>.
- [19] C.J. Esposito, J.L. Tangorra, B.E. Flammang, G. V. Lauder, A robotic fish caudal fin: effects of stiffness and motor program on locomotor performance, *J. Exp. Biol.* 215 (2012) 56–67. <https://doi.org/10.1242/jeb.062711>.
- [20] S. Alben, P.G. Madden, G. V. Lauder, The mechanics of active fin-shape control in ray-finned fishes., *J. R. Soc. Interface*. 4 (2007) 243–56. <https://doi.org/10.1098/rsif.2006.0181>.

- [21] G. V. Lauder, P.G.A. Madden, J.L. Tangorra, E. Anderson, T. V. Baker, Bioinspiration from fish for smart material design and function, *Smart Mater. Struct.* 20 (2011). <https://doi.org/10.1088/0964-1726/20/9/094014>.
- [22] K.H. Low, Modelling and parametric study of modular undulating fin rays for fish robots, *Mech. Mach. Theory.* 44 (2009) 615–632. <https://doi.org/10.1016/j.mechmachtheory.2008.11.009>.
- [23] R. Gliva, M. Mountoufaris, N. Spyridakis, M. Sfakiotakis, Development of a bio-inspired underwater robot prototype with undulatory fin propulsion, *Proc. NHIBE.* (2015) 81–86. <https://pdfs.semanticscholar.org/8adf/dbed1c878b5045aa38cb3068b8f761d5e3cf.pdf>.
- [24] B.A. Chadwell, E.M. Standen, G. V. Lauder, M.A. Ashley-Ross, Median fin function during the escape response of bluegill sunfish (*Lepomis macrochirus*). II: Fin-ray curvature, *J. Exp. Biol.* 215 (2012) 2881–2890. <https://doi.org/10.1242/jeb.068593>.
- [25] N.K. Taft, B.N. Taft, Functional implications of morphological specializations among the pectoral fin rays of the benthic longhorn sculpin, *J. Exp. Biol.* 215 (2012) 2703–2710. <https://doi.org/10.1242/jeb.063958>.
- [26] J.L. Tangorra, S.N. Davidson, I.W. Hunter, P.G.A. Madden, G. V. Lauder, H. Dong, M. Bozkurtas, R. Mittal, The development of a biologically inspired propulsor for unmanned underwater vehicles, *IEEE J. Ocean. Eng.* 32 (2007) 533–550. <https://doi.org/10.1109/JOE.2007.903362>.
- [27] G. Liu, Y. Ren, H. Dong, O. Akanyeti, J.C. Liao, G. V. Lauder, Computational analysis of vortex dynamics and performance enhancement due to body-fin and fin-fin interactions in fish-like locomotion, *J. Fluid Mech.* 829 (2017) 65–88. <https://doi.org/10.1017/jfm.2017.533>.
- [28] G. Shi, Q. Xiao, Q. Zhu, W. Liao, Fluid-structure interaction modeling on a 3D ray-strengthened caudal fin, *Bioinspir. Biomim.* 14 (2019) 036012. <https://doi.org/https://doi.org/10.1088/1748-3190/ab0fbc>.

- [29] W. Liao, J. Cai, H.M. Tsai, A multigrid overset grid flow solver with implicit hole cutting method, *Comput. Methods Appl. Mech. Eng.* 196 (2007) 1701–1715.
<https://doi.org/10.1016/j.cma.2006.09.012>.
- [30] A. Jameson, W. Schmidt, E.L.I. Turkel, Numerical solution of the Euler equations by finite volume methods using Runge Kutta time stepping schemes, 14th Fluid Plasma Dyn. Conf. (1981). <https://doi.org/doi:10.2514/6.1981-1259>.
- [31] A. Jameson, Time Dependent Calculations Using Multigrid, with Applications to Unsteady Flows Past Airfoils and Wings, AIAA 10th Comput. Fluid Dyn. Conf. (1991). <https://doi.org/10.2514/6.1991-1596>.
- [32] B.S.H. Connell, D.K.P. Yue, Flapping dynamics of a flag in a uniform stream, *J. Fluid Mech.* 581 (2007) 33–67. [https://doi.org/DOI: 10.1017/S0022112007005307](https://doi.org/DOI:10.1017/S0022112007005307).
- [33] Q. Zhu, Numerical simulation of a flapping foil with chordwise or spanwise flexibility, *AIAA J.* 45 (2007) 2448–2457. <https://doi.org/10.2514/1.28565>.
- [34] P. Causin, J.F. Gerbeau, F. Nobile, Added-mass effect in the design of partitioned algorithms for fluid-structure problems, *Comput. Methods Appl. Mech. Eng.* 194 (2005) 4506–4527. <https://doi.org/10.1016/j.cma.2004.12.005>.
- [35] C. Farhat, M. Lesoinne, Two efficient staggered algorithms for the serial and parallel solution of three-dimensional nonlinear transient aeroelastic problems, *Comput. Methods Appl. Mech. Eng.* 182 (2000) 499–515.
[https://doi.org/10.1016/S0045-7825\(99\)00206-6](https://doi.org/10.1016/S0045-7825(99)00206-6).
- [36] G.S.L. Goura, K.J. Badcock, M.A. Woodgate, B.E. Richards, A data exchange method for fluid-structure interaction problems, *Aeronaut. J.* 105 (2001) 215–221.
<https://doi.org/10.1017/S0001924000025458>.
- [37] M. Sadeghi, F. Liu, K.L. Lai, H.M. Tsai, Application of Three-Dimensional Interfaces for Data Transfer in Aeroelastic Computations, 22nd Appl. Aerodyn. Conf. Exhib. (2004) 1–30. <https://doi.org/doi:10.2514/6.2004-5376>.
- [38] R. Mittal, H. Dong, M. Bozkurtas, G. V. Lauder, P. Madden, Locomotion with flexible propulsors: II. Computational modeling of pectoral fin swimming in sunfish, *Bioinspiration and Biomimetics*. 1 (2006) S35.
<https://doi.org/10.1088/1748-3182/1/4/S05>.

- [39] H. Dong, M. Bozkurttas, R. Mittal, P. Madden, G. V. Lauder, Computational modelling and analysis of the hydrodynamics of a highly deformable fish pectoral fin, *J. Fluid Mech.* 645 (2010) 345–373.
<https://doi.org/10.1017/S0022112009992941>.
- [40] R. Li, Q. Xiao, Y. Liu, J. Hu, L. Li, G. Li, H. Liu, K. Hu, L. Wen, A multi-body dynamics based numerical modelling tool for solving aquatic biomimetic problems, *Bioinspiration and Biomimetics*. 13 (2018) 056001. <https://doi.org/10.1088/1748-3190/aacd60>.
- [41] Q. Xiao, W. Liao, Numerical investigation of angle of attack profile on propulsion performance of an oscillating foil, *Comput. Fluids*. 39 (2010) 1366–1380.
<https://doi.org/10.1016/j.compfluid.2010.04.006>.
- [42] Q. Xiao, W. Liao, S. Yang, Y. Peng, How motion trajectory affects energy extraction performance of a biomimic energy generator with an oscillating foil?, *Renew. Energy*. 37 (2012) 61–75. <https://doi.org/10.1016/j.renene.2011.05.029>.
- [43] W. Liu, Q. Xiao, F. Cheng, A bio-inspired study on tidal energy extraction with flexible flapping wings, *Bioinspir. Biomim.* 8 (2013) 36011–16.
<https://doi.org/10.1088/1748-3182/8/3/036011>.
- [44] W. Liu, Q. Xiao, Q. Zhu, Passive Flexibility Effect on Oscillating Foil Energy Harvester, *AIAA J.* 54 (2016) 1172–1187. <https://doi.org/10.2514/1.J054205>.
- [45] G. Shi, Q. Xiao, Q. Zhu, A study of 3D flexible caudal fin for fish propulsion, in: *Proc. 36th Int. Conf. Offshore Mech. Arct. Eng.*, Trondheim, Norway, 2017.
<http://dx.doi.org/10.1115/OMAE2017-61528>.
- [46] G. V. Lauder, P.G.A. Madden, Fish locomotion: Kinematics and hydrodynamics of flexible foil-like fins, *Exp. Fluids*. 43 (2007) 641–653.
<https://doi.org/10.1007/s00348-007-0357-4>.